A&A, 710, A262 (2026)
https://doi.org/10.1051/0004-6361/202660026

Astronomy & Astrophysics

Discovery of phase-locked intermittent brightenings in PSR B1919+21

S. Gulyaev[1,⋆], W. van Straten[1,2], C. Tiburzi[3,4], N. Primak[1], and V. Osherovich[5]

[1] Radio Astronomy Modelling and Statistics, Auckland University of Technology, Auckland, New Zealand
[2] Manly Astrophysics, 15/41-42 East Esplanade, Manly, NSW 2095, Australia
[3] INAF – Osservatorio Astronomico di Cagliari, via della Scienza 5, 09047 Selargius (CA), Italy
[4] INAF – Osservatorio Astronomico di Brera, Via Emilio Bianchi 46, I-23807 Merate, Italy
[5] NASA Goddard Space Flight Center-CUA, Retired, Code 673, Greenbelt, MD 20771, USA

Received 24 March 2026 / Accepted 18 May 2026

ABSTRACT

Context. In single-pulse observations of PSR B1919+21, we identify a previously unreported emission phenomenon, which we term phase-locked intermittent brightenings (PLIBs).

Aims. We aim to characterise the phenomenology and polarimetric properties of PLIBs and to explore possible physical interpretations of their origin.

Methods. Using highly sensitive, high time-resolution polarimetric observations of PSR B1919+21 obtained with the Arecibo Observatory, we analysed flux-density variations, pulse-phase stability, and polarisation-vector trajectories in the Stokes Q–U plane, with particular emphasis on episodes of enhanced emission.

Results. Phase-locked intermittent brightenings are characterised by flux enhancements up to an order of magnitude above the mean level, occurring intermittently but at a fixed rotational phase ($l = -5°$). They appear in both polarised and unpolarised emission and are associated with a ~90° change in the linear polarisation position angle, a transition of the Q–U vector from quadrant IV to quadrant II, and a reversal in the handedness of circular polarisation (Stokes V). Following a PLIB event, the Q–U vector executed a complete 360° clockwise rotation before returning to quadrant II; the characteristic Q–U-plane 'torus' structure at $l = 0°$ is likewise consistently confined to quadrant II.

Conclusions. We interpret PLIBs as signatures of spatially localised but temporally intermittent processes operating within the neutron-star magnetosphere. Possible mechanisms include magnetic reconnection or surface instabilities, acting within a magnetic configuration that can be represented schematically as a double-helix structure embedded in a cylindrical magnetic tube. Within this phenomenological framework, the rotation of the double-helix structure with a period of $2\,P_3$ provides a qualitative explanation for the observed evolution of the polarisation plane. Meanwhile, the rotational distortion of magnetic field lines associated with the neutron star's spin offers a plausible interpretation of the observed orthogonal polarisation mode transitions. The occurrence and modulation properties further suggest that the underlying structure has relatively low magnetic helicity. Overall, we propose a phenomenological framework that integrates these elements and provides a unified, qualitative interpretation of the emission and polarisation behaviour associated with PLIBs.

Key words. magnetic fields – polarization – radiation mechanisms: non-thermal – methods: data analysis – stars: neutron – pulsars: individual: PSR B1919+21

1. Introduction

One of the most extreme manifestations of pulsar radio emission is the phenomenon of giant pulses (GPs), characterised by intense, short-duration bursts that can exceed the average pulse intensity by several orders of magnitude. First discovered in the Crab pulsar (PSR B0531+21) (Staelin & Reifenstein 1968), GPs have since been observed in a small subset of pulsars, including the millisecond pulsars PSR B1937+21 (Wolszczan et al. 1984) and PSR B1821–24 (Romani & Johnston 2001). These pulses exhibit such unique properties as extremely short timescales (ranging from nanoseconds to microseconds) (Hankins et al. 2003), high brightness temperatures (Cordes et al. 2004), and in many cases, a power-law distribution of pulse energy (Cognard et al. 1996).

While the physical mechanism behind GPs remains an open question, several theoretical models have been proposed, including plasma instabilities (Lyutikov 2007), coherent curvature radiation (Melrose & Gedalin 1999), and magnetic reconnection events in the pulsar magnetosphere (Uzdensky & Spitkovsky 2014). The extreme nature of GPs makes them valuable probes of pulsar emission physics and magnetospheric conditions, but their rarity and variability pose observational challenges.

In this work, we report on a class of bright pulses detected in pulsar observations, which exhibit some – but not all – of the characteristics associated with classical GPs. These pulses appear approximately every 4–20 rotations, show a brief (5–7 ms) flux density (Stokes I) enhancement up to ten times the mean pulse intensity at a fixed pulse longitude, and are accompanied by a polarisation angle (PA) swing of ~90°. Notably, the orthogonal PA transitions occur at similar initial and final polarisation states. The PA swings are accompanied by a rapid change in polarisation handedness – from right-hand circular

⋆ Corresponding author: sergei.gulyaev@aut.ac.nz

polarisation (RCP; positive Stokes V) to left-hand circular polarisation (LCP; negative Stokes V), and back to RCP.

Unlike classical GPs, which tend to be highly sporadic, these pulses show a structured and quasi-periodic behaviour, suggesting a connection to mode switching (Backer & Rankin 1980) or localized plasma processes rather than purely stochastic GP emission.

We first discovered this special population of pulses during our study of the polarisation of single pulses from PSR B1919+21 (Primak et al. 2022, hereafter Paper 1). We noticed that the longitude-resolved polarisation of a subset of single pulses exhibited multiple rotations of the PA (Gulyaev 2021, private communication). The same phenomenon was later independently discovered and reported by Cao et al. (2025). In addition to their remarkable polarisation properties (see Sect. 3.3), these special pulses are exceptionally bright (see Sect. 3.1). They also occur at times separated by multiples of the drift period, P_3 (see Sect. 3.2), and within a limited range of the drift cycle phase (Sect. 3.3).

Therefore, we introduce the term phase-locked intermittent brightenings (PLIBs) to describe emission features that occur intermittently yet recur at a fixed rotational phase (pulse longitude) and within a well-defined window of drift phase. Their phase stability, combined with their intermittent nature, points to spatially localised structures within the pulsar magnetosphere, while the underlying physical processes responsible for their activation remain temporally variable.

In this paper, we present a detailed observational characterisation of PLIBs, including their statistical properties and polarisation behaviour. We then outline a phenomenological interpretation intended to organise these observational findings and to highlight possible physical ingredients, such as orthogonal polarisation mode (OPM) switching and localised magnetospheric activity, within a phenomenological framework rather than a detailed plasma or magnetohydrodynamic (MHD) treatment. By doing so, this study aims to provide a robust observational foundation for PLIBs and to motivate future theoretical and computational work on the coupling between polarisation behaviour and pulse intensity in pulsar magnetospheres.

2. Data and processing

In Paper 1, we analysed highly sensitive observations of PSR B1919+21 obtained with the Arecibo 300 m radio telescope at 1414 MHz. These observations form part of a larger single-pulse dataset obtained with the Arecibo Radio Telescope between 1988 and 1992 at multiple frequencies, described in detail by Hankins & Rankin (2010). In the present work, we continue our analysis using the same Arecibo dataset. Throughout the analysis, we work with the full set of Stokes parameters: I, Q, U and V. We analyse a 30-minute uninterrupted observation comprising over 1.6×10^3 individual pulses. In this section, we summarise the data reduction steps applied to the original Arecibo raw data.

Note. Hereafter, we provide both longitude and bin enumerations for our dataset. Each data bin corresponds to a longitude interval of $\Delta l = 0.325°$. Given the pulsar period of $P_1 = 1.33730$ (see e.g. Hobbs et al. (2004)), one bin also represents a time interval of approximately 1.21 ms. The entire pulse window spans about 40 bins, equivalent to 13° in longitude or ∼50 ms in time.

Note. There are different conventions for defining the longitude zero point. For example, Cao et al. (2025) set the zero longitude at what corresponds to bin #80 in our data. In our work, we adopted the longitude calibration proposed in Paper 1, where we set the longitude zero point at bin #96 of our dataset. Under this calibration, the zero-point used by Cao et al. (2025) corresponds to longitude $l = -5°$ in our system.

The first stage of analysis involved modelling and subtracting the off-pulse baseline. Fig. 1 (a) shows the average off-pulse Stokes I flux density (red band) together with its quadratic-law fit (white curve). Owing to projection effects, the system equivalent flux density (SEFD) of the Arecibo observatory increases with time as the source transits away from the zenith of the dish. Stokes I fluxes of pulses near longitude $l = -5°$ (bin #80) lie well above the off-pulse noise. Subtracting the off-pulse baseline from the same longitude bins yields the flux densities plotted in Fig. 1(b).

To estimate the underlying gain variation, we next applied a Savitzky–Golay (S–G) filter to the Stokes I fluxes (red curve in Fig. 1(b)) . Unlike a simple moving-average filter, the S–G filter fits a low-order polynomial within a sliding window, preserving higher-order moments such as peak heights and curvature. This approach retains PLIBs while revealing the smooth variation in effective gain. The resulting S–G curve was then approximated with a polynomial (white curve). This effective gain correction accounts for the combined effects of antenna projection and interstellar scintillation[1]. The gain-normalised flux densities are shown in Fig. 1(c). The same gain correction was applied to all four Stokes parameters.

3. Analysis

Using the gain-normalised data described in Sect. 2, we carried out a detailed analysis of the PLIBs. We examined their intensity distribution (Sect. 3.1), periodicity (Sect. 3.2), and polarisation properties (Sect. 3.3).

3.1. PLIB intensities

We derived the mean flux density across all 1624 pulses to investigate the distribution of total, polarised, and unpolarised flux density. Figure 2 presents longitude-resolved average flux densities of these three quantities.

In all three quantities, two distinct maxima are evident: a peak near bins #80–#82 ($l = -5°$), most pronounced in the unpolarised component (right panel), and a maximum near bin #96–#98 ($l = 0°$).

Figure 3 presents total flux densities at longitude $l = -5°$ for a series of pulses shown with successive zoom levels. Some pulses are significantly brighter than the mean flux at this longitude.

To objectively define what qualifies as a PLIB event, we analyse the distributions (histograms) of total flux (Stokes I), polarised flux, P, and unpolarised flux, $I_{\rm un} = I - P$, at $l = -5°$ (bin #80) across the full dataset of 1624 pulses (Fig. 4).

These histograms allow us to distinguish the rare, bright pulses that stand out from the bulk emission. Phase-locked intermittent brightenings are defined as pulses whose fluxes lie well above the main distribution. They show very high unpolarised flux compared to the background population. Identifying these outliers provides a quantitative basis for isolating PLIBs from the broader set of ordinary pulses.

The histogram of unpolarised flux is close to Gaussian. This arises from the incoherent sum of many small, independent

[1] At 1.4 GHz, the scintillation timescale for PSR B1919+21 varies around 670–1500 pulses (Cordes 1986; Bhat et al. 1999).

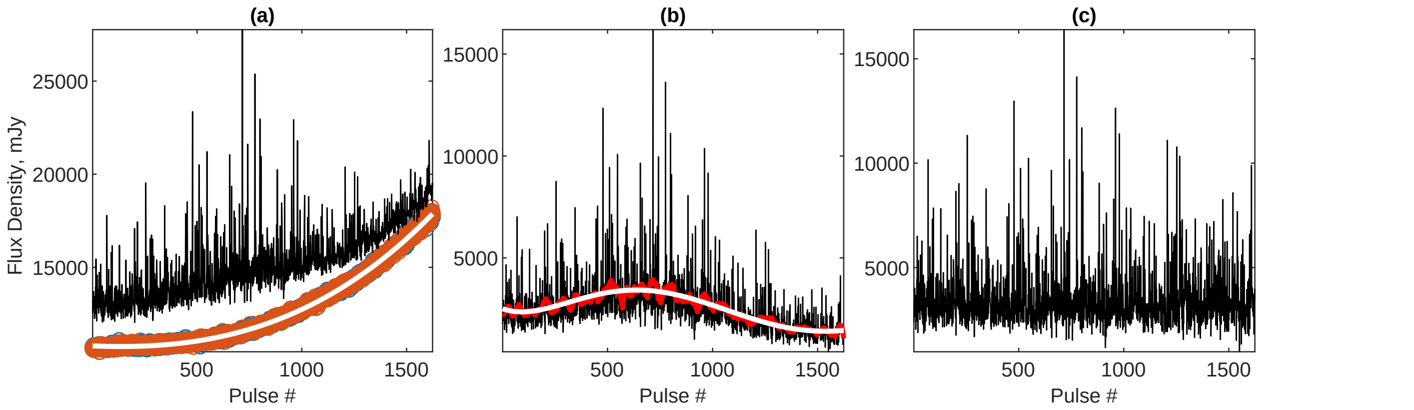

Fig. 1. Stokes I flux densities in phase bin #80 ($l = -5°$) as a function of pulse number (time). (a) Flux densities (in black) and average off-pulse flux densities (in red). The white curve denotes the quadratic-law fit to the off-pulse noise. (b) Flux densities after subtracting the off-pulse quadratic-law fit. The Savitzky–Golay (S–G) filter output is shown in red. The smooth white curve denotes a polynomial fit to the S–G result and is treated as a gain correction. (c) Flux densities after normalising with gain correction.

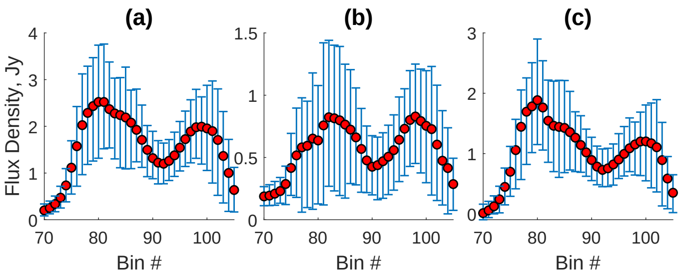

Fig. 2. Longitude-resolved flux densities averaged over 1624 pulses: total flux density (Stokes I, left panel), polarised flux density ($P = \sqrt{Q^2 + U^2 + V^2}$, centre panel), and unpolarised emission ($I_{\rm un} = I - P$, right panel). Error bars indicate one standard deviation.

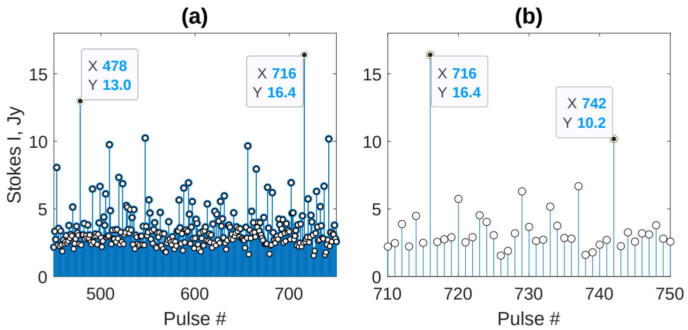

Fig. 3. Total flux density (Stokes I) in bin #80 ($l = -5°$). The y-axis shows the flux density in jansky, and the x-axis shows pulse number. Panels (a) and (b): Portions of the dataset with successive zoom levels. Some pulses (PLIBs) are well above the ~2.5 Jy mean level. The polarisation properties of some pulses marked in panel (b) are analysed in Sect. 3.3.

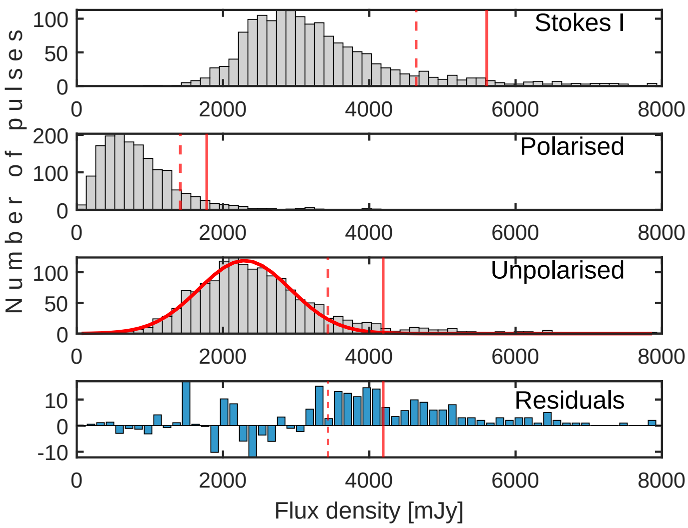

Fig. 4. Histograms of pulse flux densities for the full dataset of 1624 pulses at $l = -5°$ (bin #80). Top panel: Total flux density (Stokes I). Second panel: Polarised flux. Third panel: Unpolarised flux with a Gaussian model fit. Bottom panel: Residuals between the unpolarised flux histogram and the fitted Gaussian model. A vertical dashed red line in each panel marks the 90% threshold used in the analysis for ordinary (non-PLIBs) pulses. The solid red line in the two bottom panels mark the 6% threshold used for PLIB pulses. The x-axis shows flux density in millijansky, and the y-axis indicates the number of pulses within each histogram-bin (bin width = 130 mJy). All panels share the same x-axis range (0–8000 mJy).

emission contributions. A small excess at high fluxes appears as a distinct bump, which we attribute to the PLIB population. In contrast, the polarised flux distribution is strongly non-Gaussian. It rises steeply at low values and exhibits a heavy high-flux tail. This shape is expected, since the polarised flux represents the magnitude of the Stokes vector. When only linear components (Q, U) are considered, the resulting distribution is Rayleigh-like. By contrast, when all three components (Q, U, V) are included, it follows a Maxwell–Boltzmann-like form. The additional high-flux tail reflects genuine astrophysical events, such as sporadic mode dominance and coherent polarised bursts, which deviate from the purely statistical behaviour of random polarisation.

The distribution of total flux (Stokes I) is also asymmetric and non-Gaussian. This is naturally explained by its being the sum of the polarised and unpolarised components: the unpolarised part is nearly Gaussian, whereas the polarised part is highly skewed, and their combination inherits the asymmetry of the latter.

We fitted a Gaussian to the unpolarised flux distribution (solid red contour in the third panel) and calculated the residuals, that is the excess counts relative to the Gaussian model (the lower panel of Fig. 4). A vertical dashed red line in each panel marks the 10% threshold used in the analysis. It corresponds to

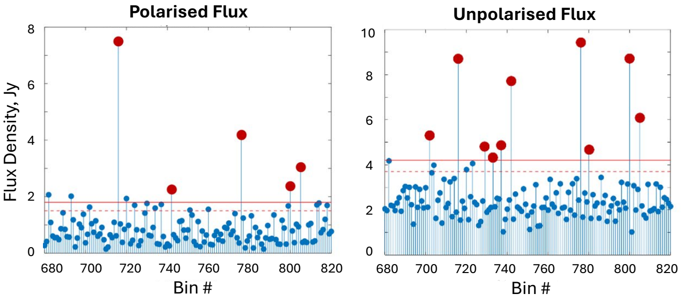

Fig. 5. Set of 140 pulses at longitude $l = -5°$ polarised (left) and unpolarised flux (right). Flux density is given in jansky (y-axis) vs pulse number (x-axis). The horizontal red lines correspond to the brightest 6% (solid line) and 10% (dashed line) limits for each component of flux. The red dots in the right panel mark the ten brightest (PLIBs) pulses. Of these, only five appear above the threshold in the left panel.

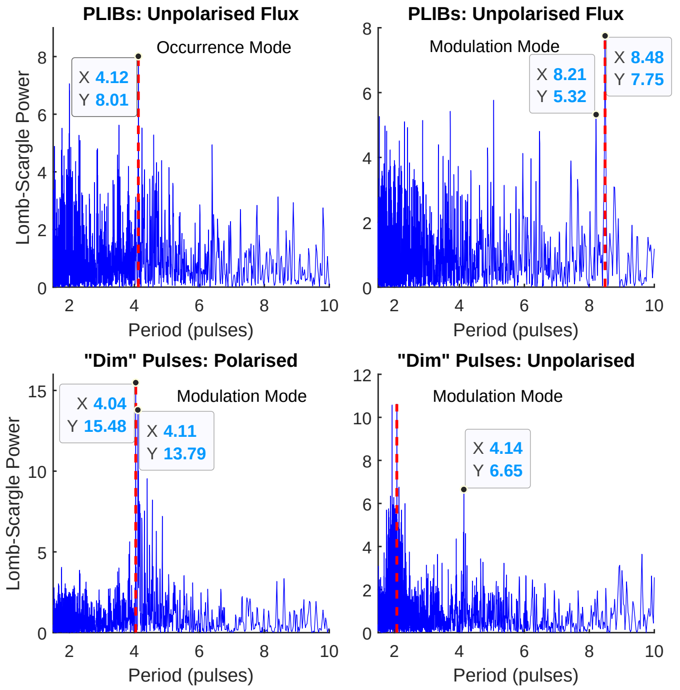

Fig. 6. Lomb–Scargle (LS) spectra of pulses at $l = -5°$ (bin #80). Top panels: Bright (PLIBs) pulses, shown for occurrence mode (left) and modulation mode (right) – both for unpolarised emission. Bottom panels: Dim (non-PLIBs) pulses, polarised flux (left), and unpolarised flux (right) – both in modulation mode. In occurrence mode, PLIBs show clear periodicity at $P_3 \approx 4.1–4.2\,P_1$, while in modulation mode, they display their strongest features at $2\,P_3$, indicating flux alternation. For dim pulses, the polarised component shows a broadened cluster of very strong peaks around P_3, whereas the unpolarised component exhibits only a weak feature at P_3. A symmetric comb near $P = 2\,P_1$ in the bottom-right panel is identified as instrumental.

Stokes I limit of 4.7 Jy and unpolarised flux limit of 3.5 Jy. The number of residual counts to the right of the vertical dashed red line is 162 (10% of the total sample). However, not all of this excess can be attributed to PLIBs.

To apply a conservative criterion, we focused on the unpolarised component I_{un} and classified the brightest 6% (97 pulses) in the I_{un} distribution as PLIBs. This corresponds to $I_{un} > 4.2$ Jy (or $I > 5.6$ Jy). Some pulses in the intermediate range 3.7–4.2 Jy in I_{un} (4.9–5.6 Jy in I) may also belong to this class.

Boolean analysis applied to the full set of 1,624 pulses recovers 97 PLIBs using the I_{un}-based 6% criterion ($I_{un} > 4.2$ Jy). The same number of pulses (97) also exceed the $I > 5.6$ Jy threshold, but the overlap is incomplete: 76 pulses (78%) satisfy both cuts; 21 PLIBs as defined by the polarisation of the single pulses (see Sect. 3.3) are missed by the total-flux selection; conversely, 21 pulses with high I are not PLIBs. Among the 97 PLIBs, 43 (44%) have polarised flux below the top-6% cut, indicating that their polarised component is ordinary or moderate. This demonstrates that the I_{un}-based criterion is more selective and should be regarded as primary, whereas thresholds based on I or P alone can misclassify a substantial fraction of events.

The utility of the unpolarised flux criterion is illustrated in Fig. 5 where we use a set of 140 pulses at longitude $l = -5°$. The panels show polarised flux (P) and unpolarised flux ($I_{un} = I - P$). In the right panel (unpolarised flux), the red dots mark all the brightest (PLIBs) pulses according to the 6% threshold – ten pulses altogether. There are only five pulses of this selection above the polarised flux's 6% criterium (left panel). By comparison, Stokes I (not shown here) has eight pulses that overlap with ten selected unpolarised pulses. In summary, in terms of their brightness (flux density), PLIBs are best defined as pulses with an unusually bright unpolarised component, regardless of their total or polarised flux, making the I_{un} threshold the most reliable PLIBs identification criterion.

3.2. PLIB periodicity

We analysed the periodic behaviour of pulses at $l = -5°$ using the Lomb–Scargle (LS) method in two complementary modes. In the 'occurrence mode', pulses are represented as a binary sequence: '1' for pulses above a threshold and '0' otherwise. The LS spectrum then tests whether the occurrence times of strong pulses are periodic. This approach is sensitive to clustering of rare, bright events. In 'modulation mode', the LS is directly applied to flux values, probing oscillatory modulation in pulse intensity rather than just the timing of threshold crossings.

The results of the Lomb–Scargle analysis for bright and dim pulse subsets at $l = -5°$ are summarised in Fig. 6.

The statistical significance of peaks in the LS spectrum can be quantified using the false alarm probability (FAP),

$$\mathrm{FAP} = 1 - (1 - e^{-z})^M ,$$

where z is the LS power and M the effective number of independent frequencies, which scales with the number of available data points, N. For bright-pulse subsets ($N \approx 100$), a peak with $z = 8$ corresponds to FAP $\sim$ 4%, indicating moderate significance. For dim pulses ($N \approx 1500$), $z = 16$ yields FAP $\sim 10^{-4}$, which makes it statistically highly significant.

In occurrence mode (the upper-left panel in Fig. 6), the bright pulses (PLIBs; the top 6% in flux) show a clear periodicity at $P \approx 4.1–4.2\,P_1$ (P_3), with a significance $z \approx 8–9$. By contrast, in modulation mode, the unpolarised flux (PLIBs) does not peak at P_3 but shows its strongest feature at $P \approx 8.2–8.4\,P_1 \approx 2\,P_3$ (the upper-right panel in Fig. 6).

This contrast implies that the probability of PLIBs occurrence is modulated at P_3. Nevertheless, their flux amplitudes follow an alternation pattern: successive PLIBs differ in strength (high–low–high–low), producing a $2P_3$ signature. Importantly, both the 'high' and 'low' pulses remain above the adopted PLIBs threshold, so occurrence mode captures the underlying P_3 clock while the modulation mode reveals the alternation. Together,

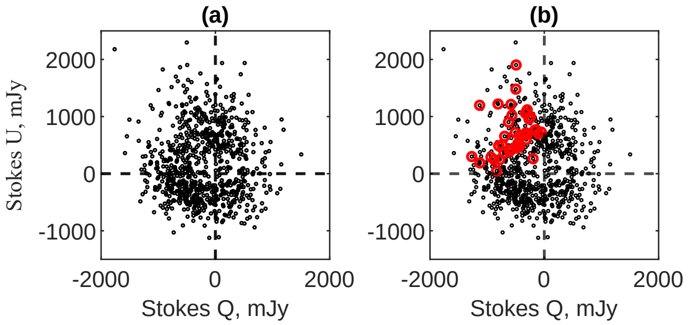

Fig. 7. (a) Absolute values of Q and U plotted for 800 pulses at longitude $l = 0°$ (bin 96), forming a characteristic torus shape in the Q–U plane. (b) Same plot with the red circles marking the PLIB pulses – those with Stokes $I > 5000$ mJy as measured at $l = -5°$ (bin #80). All of these appear in quadrant II in the $Q - U$ plot for $l = 0°$ (bin 96).

these results indicate that PLIB pulses preserve the same organising cycle as ordinary emission but display a distinct secondary modulation. (See Fig. 14 in Sect. 4.)

For dim pulses (the bottom 90% of the population, excluding the 6–10% transition interval), the picture is different (Fig. 6, bottom panels). The polarised flux exhibits a broad cluster of peaks around P_3 (4.04–4.39 P_1), with very high significance (up to $z \approx 16$). This broadening suggests less coherent modulation than in the PLIBs case, perhaps due to temporal drifts, longitude dependence, or overlapping quasi-periodic processes (Castelltort Schnaas 2022). For the unpolarised flux, the P_3 feature is much weaker ($z \approx 6.6$) but still present, consistent with the idea that curvature radiation produces both a strongly polarised component carrying the coherent modulation and a partially unpolarised residual, where the same modulation is diluted by noise and incoherent contributions.

The unpolarised dim-pulse spectrum also shows a symmetric comb of peaks centred on $f = 0.5$ (period $P = 2P_1$) but without a corresponding carrier. Diagnostic checks indicate this is likely instrumental- and/or pipeline-related in origin rather than astrophysical, and we therefore exclude it from further interpretation.

3.3. PLIB polarisation properties

In Paper 1, we analysed the intensity maximum around $l = 0°$ (bin #96), and found that the PA, ψ, in individual pulses remains nearly constant ('frozen') for about 5–6 ms (bins #94–#98; $-0.8° < l < 0.8°$). From pulse to pulse, this frozen-PA region shifts by $\Delta\psi \approx 40°$–$45°$ clockwise, producing a systematic, periodic rotation that completes 180° with a period $P_3 \approx 4.1$–$4.2\,P_1$. An animation illustrating this behaviour is provided in Paper 1[2]. This drift phase-locked PA rotation generates the toroidal structure seen in the single-pulse Q–U scatter plot near $l = 0°$ (bin #96) – reproduced in Fig. 7(a).

In this work, we focused on the other intensity maximum, near $l = -5°$ (bin #80), starting with its connection to the $l = 0°$ (bin #96) torus feature examined in Paper 1.

As illustrated in Fig. 7(b), all pulses with high total flux density (Stokes $I > 5000$ mJy) at $l = -5°$ (bin #80) are found in the same quadrant II of the Q–U plane plotted for $l = 0°$. The bins forming the torus structure normally circulate through all quadrants. However, during PLIBs events, they are consistently located in quadrant II, which can also be seen in selected PLIB pulses (Fig. 9, right panels) and in the P_3-folded PA diagram (Fig. 10, left). This spatial and polarimetric correspondence suggests a physical link between the two longitude regions, which we discuss in Sect. 4 ('Phenomenological model').

To further explore the polarisation behaviour of PLIBs, we analysed the brightest events, defined as pulses with unpolarised flux exceeding the 6% PLIB threshold. Figure 8 shows an example of such a PLIB event occurring in one of the pulses (#716) from the analysed dataset.

This PLIB occurs within the range of bins #77–#82, peaking in total flux density, I, and unpolarised flux, $I_{\rm un}$, at bin #80. The observed time duration of an individual PLIB is approximately 5–7 milliseconds (i.e. 4–6 bins of our data, or about 1–1.5° in pulse longitude). For comparison, we show polarisation and Stokes parameters for two neighbouring (non-PLIB) pulses: #715 and #717, which do not show any brightening. In pulse #716, the PLIB flux density reaches 17 Jy in Stokes I, which is ~7 times higher than the average flux in bin #80 (~2.5 Jy).

Figure 9 shows polarisation evolution on the Q–U plane for three typical PLIB pulses.

In the left panels, the polarisation tracks begin in quadrant IV (bin #79/80) and end in quadrant II (bin #81/82) showing a clear OPM transition. The unpolarised flux exhibits a sharp, narrow peak, typically in bin #80, occurring just before or at the onset of the OPM switch (see the unpolarised flux panel in Fig. 8). The increased flux in bin #80 is depolarised owing to the OPM switch; that is, the combination of the modes (either an incoherent superposition or composition) depolarises the sample mean Stokes parameters integrated over this longitude interval (van Straten & Tiburzi 2017). In contrast, the tracks in the right panels of Fig. 9 start and end in quadrant II but traverse all four quadrants (II → I → IV → III → II), indicating a full rotation of the polarisation vector before returning to the same PA. This confirms that the PA associated with quadrant II plays a special role, which must be incorporated into any phenomenological model (Sect. 4).

The coincidence of these quadrant transitions is further supported by analysis of the PA and Stokes I. Figure 10 presents the drift-phase folded PA (left) and total flux I (right). Folding both PA and I with a period of $4\,P_3$ (rather than P_3) produces four consecutive realisations of the modulation pattern, improving phase discrimination. Because folding averages over many pulses, the observed I amplitudes are lower than in individual PLIBs events and the maxima appear diluted, reflecting that PLIBs do not occur in every P_3 cycle.

Despite this averaging, OPM transitions consistently cluster near bin #80 (vertical white line) and are phase-aligned with Stokes I maxima, demonstrating strong drift phase coherence between enhanced emission and OPM switching (horizontal white lines). Furthermore, the 'torus' region (bins #93–#98) shows the same PA as the orthogonal mode that emerges at the bin-80 transition, suggesting a stable linkage between these regions across the emission cycle. By contrast, between PLIB pulses (between the horizontal white lines in Fig. 10, left), only smooth pre-OPM PA values (green colour) are present, with no trace of the orthogonal mode, highlighting that OPM switching is confined to discrete P_3 phases.

3.4. Comparison and contrast with other phenomena

The population of PLIB pulses share some features with previously discovered phenomena of radio pulsar emission and also differ in some key aspects. First, we note that PLIBs differ

[2] The animation is available at https://www.aanda.org/articles/aa/olm/2022/01/aa40811-21/aa40811-21-mov1-olm.zip

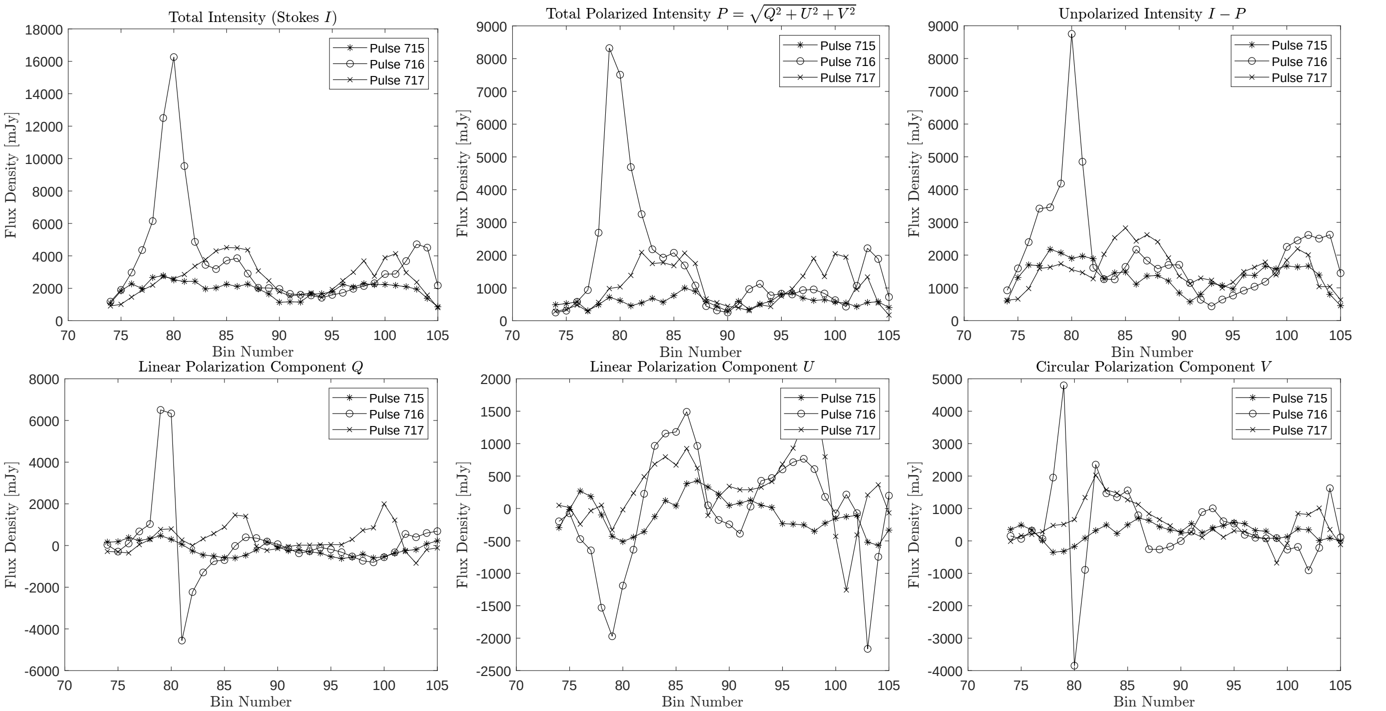

Fig. 8. Example of a PLIB pulse (#716). Top row: Total (I), polarised (P), and unpolarised (I_{un}) fluxes for pulses #715–717. Bottom row: Corresponding Stokes parameters Q, U, and V.

significantly from GPs. Phase-locked intermittent brightening pulses have durations of the order of milliseconds and amplitudes that are ∼5–10× the average flux. In contrast, GPs have durations of the order of nanoseconds and many orders of magnitude greater amplitudes. On an angular scale, PLIBs are similar to the giant micropulses observed in the Vela pulsar, which have typical half-widths around 400 μs (about 1.6° in pulse longitude) and also occur on the leading edge of the mean pulse profile (Johnston et al. 2001). However, the brightest giant micropulses are more than 130× brighter than the mean flux density at the pulse longitude of their emission, and they show no sign of OPM. In this regard, PLIBs are more similar to the 'bump' emission observed on the trailing edge of the Vela pulsar's mean profile. At 1413 MHz, the 21 pulses that contribute to the bump are more than ten times brighter than the mean profile at their longitude, they occur quasi-periodically, and they are unpolarised due to OPM emission (Johnston et al. 2001).

The connection between the occurrence of OPM and increased intensity modulation has been noted for other pulsars (McKinnon 2004). In the PLIB events of PSR B1919+21, OPM switching is observed to coincide with exceptionally bright pulses that occur at a particular drift phase. Handedness reversals in circular polarisation have also been reported for other pulsars (e.g. Rankin 1983; Navarro et al. 1997; Xilouris et al. 1998). In PLIBs, this reversal happens close to the beginning of the pulse window and always at the same longitude ($l = -5°$, bins #78–#82).

The unpolarised flux selection criterion introduced in Sect. 3.1 is nearly the opposite of the selection criterion applied by Johnston et al. (2024). After integrating only pulses that are more than 80% polarised, the number of pulsars in their sample exhibiting the S-shaped swing of ψ predicted by the rotating vector model (RVM Radhakrishnan & Cooke 1969) increase from 40% to 95%. In contrast, the PLIB pulses selected based on peak unpolarised flux exhibit a full rotation of the Stokes parameters that cannot be explained by the RVM. In this regard, PLIBs are more similar to the single pulses of PSR J2251−3711 discovered by Morello et al. (2020). After the OPM transition in bins #80/81 and before the appearance of the torus in bins #95/96, that is, within the interval of bins #82–#94, the polarisation vector in the Q–U plane typically completes a full 360° clockwise rotation (Fig. 9, right panels). This corresponds to a 180° rotation of ψ, followed by a return to its initial orientation (as seen at bin #82). Cao et al. (2025) report similar sweeps of ψ over 180°–540° in over one third of the single pulses of PSR B1919+21, confirming an earlier finding by Gulyaev (2021, private communication). The incidence of this polarisation feature increases dramatically to about 80% of all PLIB pulses; however, although the single pulses studied in this work include examples of $|\Delta\phi| \sim 540°$, and both clockwise and counter-clockwise rotation, the PLIB pulses represent a subset that exhibit ∼180° clockwise rotation of ψ (Fig. 9, right panels).

Neither Primak et al. (2022) nor Cao et al. (2025) reported any phase-locked, quasi-periodically recurring bright features consistent with PLIBs. Two factors likely contributed to this:

1. Use of relative intensities. Cao et al. (2025) primarily analysed relative quantities such as Q/I, P/I, and V/P, whereas the present work uses gain-calibrated absolute Stokes parameters, making PLIBs easier to identify in the unpolarised emission.
2. Pulse integration approach. Primak et al. (2022) mainly analysed data integrated over all pulses. Although PLIBs can affect the integrated polarisation profile, they occur in only about 5–10% of pulses, so their signatures are substantially diluted or masked by the average emission.

4. Phenomenological model

4.1. Observational features to be explained

The observed features of PLIB events described in the previous section place strong constraints on any phenomenological

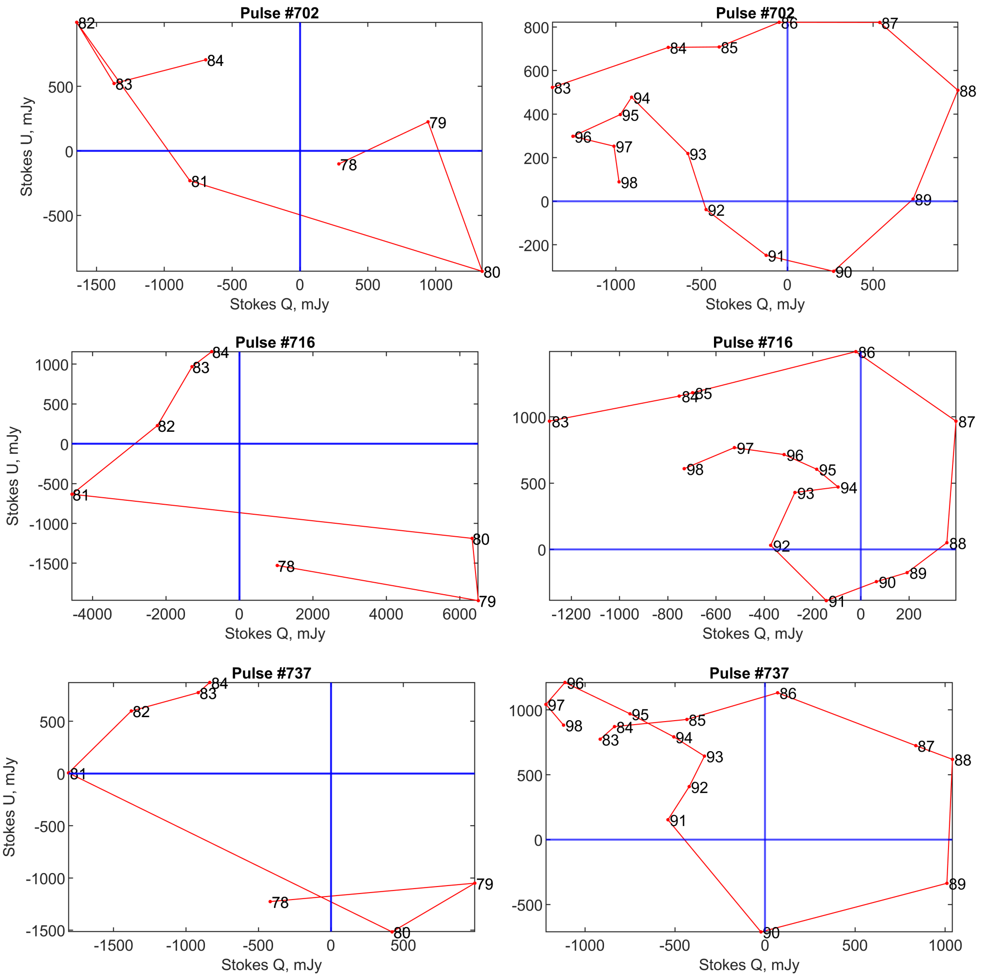

Fig. 9. Evolution of polarisation properties of selected PLIB pulses on the Q–U plane. The plotted pulses are among the brightest PLIBs, with unpolarised flux exceeding the 6% threshold. Left: Bins #78–#84 (longitudes $l = -5.5°$ to $-3.5°$). Right: Bins #83–#98 ($l = -3.5°$ to $+1.5°$). Note that the scales in the left and right panels are different.

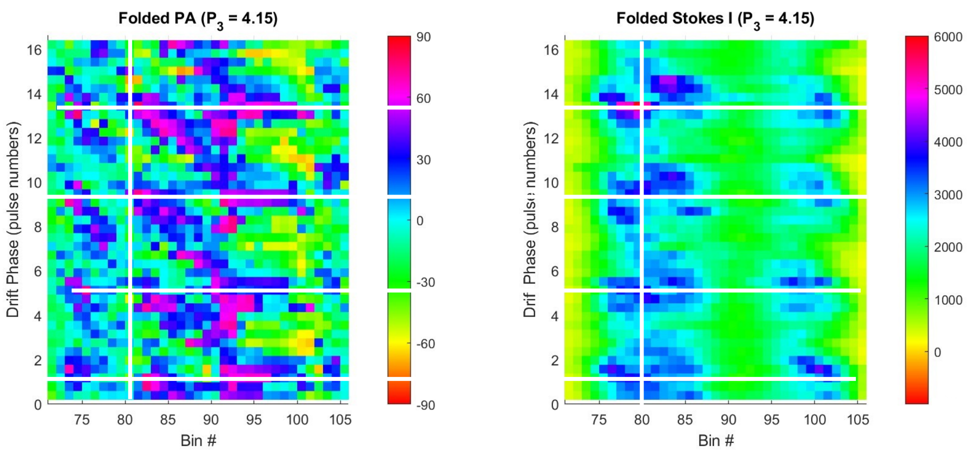

Fig. 10. PA (left) and total flux I (right) folded with a period of $4\,P_3$. The horizontal white lines, which recur with a period of P_3, mark pulses in which PLIBs, OPM transitions in bins #80–#81, and the 'torus' regions in bins #93–#98 co-occur within the same pulse. The vertical white lines at bin #80 in both panels highlight the phase coherence between enhanced emission (PLIBs) and OPM switching.

model proposed to explain them. When developing a model of the pulsar magnetosphere and its radiation mechanisms, the following interrelated PLIB features should be considered together:

1. Bins #79–#82 ($l = -5° \pm 0.8°$): Exceptionally bright pulses occur quasi-periodically, with a period near $2P_3$. These pulses exhibit an OPM switch, in which the linear polarisation switches ($\Delta\psi \approx 90°$) from quadrant IV to quadrant II in the Q–U plane, and the circular polarisation switches from RCP to LCP. Owing to the superposition of OPMs results, these bright pulses are unpolarised in bin #80, just before the OPM transition.
2. Bins #83– #93 ($-4.2° < l < -0.8°$): The polarisation vector in the Q–U plane undergoes a complete 360° clockwise rotation, starting and ending in quadrant II.
3. Bins #94–#98 ($l = 0° \pm 0.8°$): The bins forming the characteristic 'torus' structure consistently fall within quadrant II of the Q–U plane.

This description is to some extent idealised – while the features outlined above tend to occur together, their co-occurrence is not guaranteed. It is possible that deviations from the expected idealised pattern arise from the subpulse drift period, P_3. If P_3 were exactly $4P_1$, the pattern would repeat every fourth pulse. If it were $4.2P_1$, repetition would occur every 21st pulse. However, the actual value of P_3 appears to deviate slightly from these ratios and may itself vary over time, as indicated by the broad cluster of peaks near P_3 in Fig. 6. As a result, the appearance of the full pattern is quasi-regular and not quite predictable. It is likely further complicated and potentially obscured by the (partially) coherent superposition of OPMs (e.g. Gangadhara 1997; Oswald et al. 2023).

4.2. Physical assumptions

To interpret selected radiation and polarisation properties of PSR B1919+21, we introduce a phenomenological model, conceptually similar to the carousel picture. The model is intentionally qualitative and supported by schematic illustrations, rather than by detailed plasma or MHD calculations. Its purpose is to provide a physically motivated framework for interpreting and contextualising the observed properties of PLIBs and to guide future, more comprehensive modelling efforts.

In our model we adopted a spatial (rather than temporal) interpretation of observed millisecond-scale variations in emission and polarisation. That is, these variations reflect the 'scanning' of a pre-existing emission structure as the pulsar rotates rather than rapid physical changes in the pulsar magnetosphere on short timescales (Edwards & Stappers 2003). The observed emission appears through a narrow visibility window, defined by the line of sight sweeping across the emission cone near the magnetic pole (Lyne & Manchester 1988).

We adopted curvature radiation as the primary emission mechanism, which is commonly invoked in models of pulsar radio emission (Ruderman & Sutherland 1975; Melrose 1978). While synchrotron radiation was not treated explicitly in this work, order-of-magnitude estimates indicate that it may lead to qualitatively similar observational signatures under the expected magnetic field strengths and particle energies (Melrose & Yuen 2016).

To interpret the observed polarisation properties of PLIBs within a phenomenological framework, we made the following assumptions:

1. We considered bound-state solutions of the equations studied by Chandrasekhar & Prendergast (1956), which permit the formation of double-helix magnetic flux-rope structures (Krat & Osherovich 1978; Osherovich et al. 2013). These structures are adopted here as a schematic representation of organised magnetospheric configurations.
2. We assumed that the double-helix magnetic-field structure undergoes rotation with the subpulse drift period P_3 (or $2\,P_3$), analogous to the rotation of spark patterns in the carousel model of subpulse drifting (Deshpande & Rankin 1999; Mitra & Rankin 2008).
3. We assumed that the rapid rotation of the neutron star leads to a rotational distortion of magnetic field lines – a drag effect. This effect is conceptually similar to the Parker spiral in the solar wind (Parker 1958) and has been explored in the context of pulsar magnetospheres (Li et al. 2012; Pétri 2020, 2021, 2022).
4. We invoked intermittent magnetic reconnection events in the inner magnetosphere, within or near the radio-emission region (Lyutikov 2003; Philippov et al. 2020) as a plausible mechanism for producing enhanced unpolarised emission and OPM transitions, all of which are well documented in pulsar emission studies (McKinnon & Stinebring 1998; Karastergiou et al. 2002).

Together, these assumptions define a phenomenological framework that motivates the illustrative model outlined in the following subsection.

4.3. Proposed model

The magnetostatic equilibrium for axisymmetrical configurations was studied by Chandrasekhar & Prendergast (1956). Johnson et al. (1958) considered the equations for magnetostatic balance between magnetic force and the gradient of gas pressure, P:

$$\frac{1}{4\pi}(\nabla \times \mathbf{B}) \times \mathbf{B} = \nabla P, \qquad \nabla \cdot \mathbf{B} = 0. \tag{1}$$

Employing a helical coordinate variable

$$\xi \equiv \kappa z - m\phi, \tag{2}$$

where κ and m are constants defining the pitch and azimuthal periodicity, respectively, they reduced Eq. (1) to a single scalar partial differential equation for the magnetic flux function $\psi(R, \xi)$:

$$\frac{1}{R}\frac{\partial^2 \psi}{\partial \xi^2} + \frac{1}{R}\frac{\partial}{\partial R}\left[\frac{R}{(\kappa^2 R^2 + m^2)}\frac{\partial \psi}{\partial R}\right] + 4\pi \frac{dP}{d\psi} + \frac{J}{(\kappa^2 R^2 + m^2)}\frac{dJ}{d\psi} + \frac{2\kappa m J}{(\kappa^2 R^2 + m^2)^2} = 0. \tag{3}$$

For a linear function $J(\psi)$ and a quadratic function $P(\psi)$, Woolley (1975) found a solution of Eq. (3) in the form of a hypergeometric function. For axisymmetric case ($m = 0$), Osherovich (1975) analysed bounded-state solutions of Eq. (1) and interpreted them as configurations with finite energy per unit length of the magnetic tube and a continuous magnetic field.

Krat & Osherovich (1978) recast Eq. (3) into a Schrödinger-like form and solved it analytically for the ground state $n = 1$, $m = 1$. This solution corresponds to a 3D double-helix structure:

$$\frac{\psi}{\psi_0} = \left[(\kappa R)^2 - 1 + X_0 \frac{\kappa R \cos \xi}{\sqrt{2}}\right] \exp\left[-\frac{(\kappa R)^2}{4}\right], \tag{4}$$

where X_0 is a dimensionless parameter controlling the degree of magnetic twist and thus the helicity content of the configuration. We refer to cases with small and large X_0 as the low-helicity and high-helicity regimes, respectively (Berger 1999).

This solution corresponds to a double-helix embedded in a cylindrical magnetic tube. The components of the magnetic field vector can be found by differentiation,

$$B_R = \frac{1}{R}\frac{\partial \psi}{\partial \xi}, \qquad m\frac{B_\varphi}{R} - \kappa B_z = \frac{1}{R}\frac{\partial \psi}{\partial R}, \tag{5}$$

and by using the relationship

$$m B_z + \kappa R B_\varphi = J. \tag{6}$$

Osherovich et al. (2013) investigated the solution for $X_0 = 5$, providing a qualitative description of the behaviour for both small and large values of X_0. Figure 11 shows isosurfaces of ψ for $X_0 = 5$, where blue is the surface with negative $\psi = -1.5$, red represents isosurface with positive $\psi = 2$, and green represents a transition zone $\psi = 0$.

To illustrate the solutions for small and large values of X_0, we present Fig. 12, which shows cross-sections of the rotating double helix for $X_0 = 2$ (left) and $X_0 = 20$ (right) at a fixed

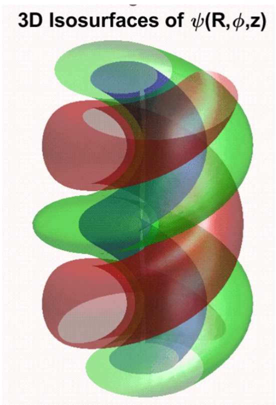

Fig. 11. Isosurfaces of ψ function for rotating double-helix solution of Eq. (4) with the helicity factor $X_0 = 5$ (isosurface with $\psi = -1.5$ in blue; isosurface with $\psi = 2$ in red; $\psi = 0$ in green).

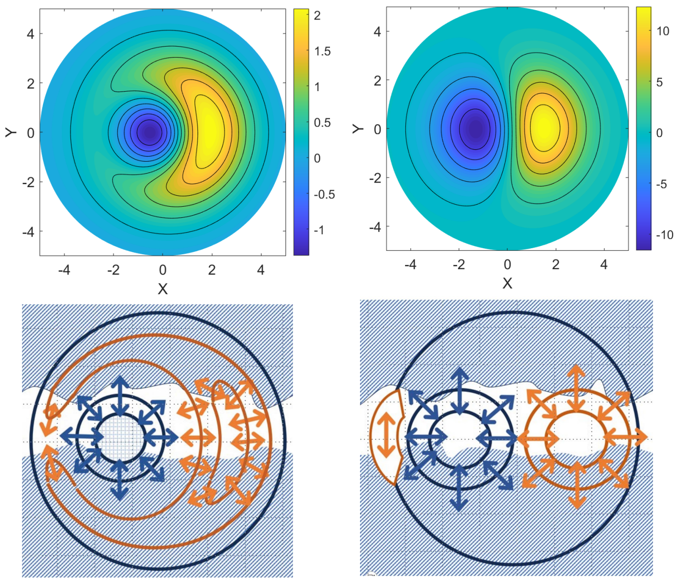

Fig. 12. Upper row: Cross-sections of the rotating double-helix solution for $X_0 = 2$ (left) and $X_0 = 20$ (right), obtained from computations based on Eq. (4). The colours represent the polarity of the magnetic flux ψ (blue for negative ψ; yellow and red for positive ψ). The thin black curves show contours of ψ. Bottom row: Schematics of the corresponding magnetic field structures, indicating the direction of the linear polarisation plane (double-sided arrows), as expected from the local magnetic-field geometry at the emission region. The shaded regions mark areas hidden from an Earth-based observer, where the curvature of the magnetic field does not allow radiation to be directed towards Earth. Observable radiation originates from the narrow horizontal white strip (window) in each bottom-row schematic.

z. The upper panels display the results of computations based on Eq. (4), while the lower panels present schematics indicating the direction of linear polarisation plane (double-sided arrows), as expected from the local magnetic-field geometry at the emission region. The colours represent the strength and polarity of the magnetic flux ψ, with blue corresponding to negative ψ, and yellow and red corresponding to positive ψ. The dashed regions in the lower panels mark areas hidden from the Earth-based observer, as the curvature of the magnetic field there prevents the radiation from being directed towards Earth. Radiation is visible only from the narrow horizontal white strip shown in the schematics.

Figure 13 illustrates a pulse-by-pulse sequence of configurations in the double-helix model when the magnetic pole is directed towards the Earth. For clarity, we adopt a double-helix rotation period of $8\,P_1$ – the corresponding 45° double-helix rotation between pulses. The vectors represent the gradient of the magnetic flux and indicate the polarisation orientation. The central white band marks the visibility window of the polar cap for the observer. Five consecutive configurations are shown for a low-helicity case ($X_0 = 2$). The pattern is asymmetric, requiring eight pulses to return to the initial configuration. In this model, the large double-sided arrow at the centre of each configuration indicates the "torus" region (bins #93–#98) and rotation of PA in this region.

This asymmetry, together with the measured periodicity of PLIBs, provides a way to infer the level of helicity (high or low X_0) in our case. As shown in Sect. 3.2, PLIB pulses exhibit a periodicity of P_3 in their occurrence pattern, and $2\,P_3$ in their flux modulation pattern. Figure 14 illustrates a possible configuration for $P_3 = 4\,P_1$. In this example, PLIB pulses occur above the detection threshold with a spacing of P_3 (occurrence mode), while their flux is modulated with a period of $2\,P_3$. The magnetic-flux configuration shown below each PLIB pulse corresponds to the magnetic field geometry during the respective PLIB pulses (configurations 1 or 5). This behaviour can be naturally explained by a low level of helicity.

Figure 15 shows schematically the effect of resistance of the surrounding medium to the motion of a fast-moving magnetic pole in the corotating reference frame. A negative gradient of gas pressure in the magnetosphere causes the double-helix structure to expand with increasing distance from the neutron star. The velocity of motion at the NS surface ($v = 100$ km/s) indicated in Fig. 15 corresponds to a NS radius of $R_{\rm NS} = 15$ km. The rotation of a magnetised neutron star through the surrounding medium induces an asymmetry in the large-scale magnetic field structure. Magnetic field lines become compressed in the direction of motion and stretched in the trailing region (Li et al. 2012).

The sequential appearance of the observed bins (pulse longitude) reflects the configuration of the magnetic field within the visibility window. In this model, longitude $l = 0°$ corresponds to the centre of azimuthal rotation of the double-helix structure. Compression of magnetic structure due to rotation of NS and interaction with the surrounding medium, makes the pulse window asymmetric: $-6° < l < +3°$. The blue plane on the right of Fig. 15 represents an idealised boundary at $l = +3°$ beyond which radiation no longer reaches Earth, due to drag-induced distortion of the magnetic field lines.

In configurations with a double-helix magnetic field topology, the interaction of the field with the surrounding medium can produce a global twist of the structure. At a fixed distance from the star, the magnetic geometry then appears to rotate in the azimuthal direction. This rotation reflects the transfer of angular momentum from the star to the ambient plasma via magnetic tension, a mechanism analogous to magnetic braking. In this picture, the double-helix appears to rotate at fixed z (Goldreich & Julian 1969; Spitkovsky 2006).

Alternative mechanisms can include internal magnetospheric dynamics or a resonant oscillation mode superimposed on the large-scale field. The system might support a resonant MHD mode or standing wave in the helical field structure, driven or modulated at $P_{\rm helix} \sim 4.1{-}4.2\,P_1$. These can occur in twisted magnetospheres, like those seen in simulations of magnetars or strongly magnetised pulsars (Parfrey et al. 2013).

In the carousel model of pulsars, proposed by Ruderman & Sutherland (1975), the rotation of the carousel is

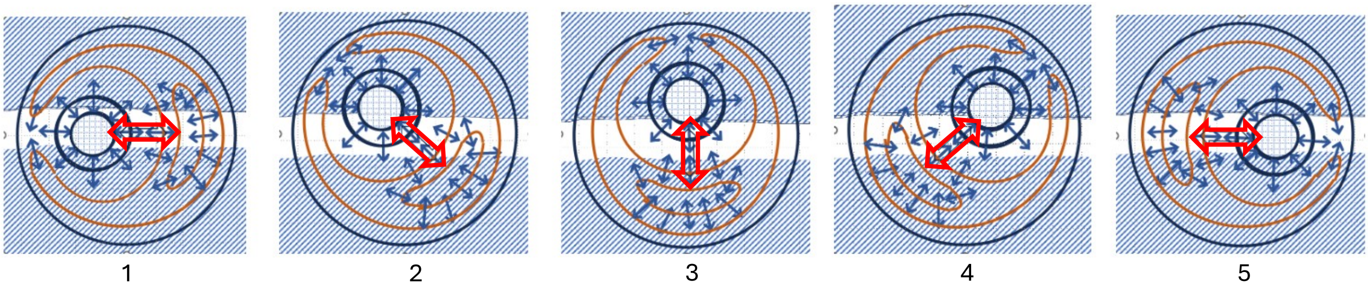

Fig. 13. Pulse-by-pulse sequence of configurations in the low-helicity double-helix model when the magnetic pole points towards the observer. A 45° double-helix rotation is applied between successive pulses, corresponding to a full rotation period of $8\,P_1$. The vectors denote the magnetic-flux gradient (polarisation orientation), and the central white band marks the observer's visibility window. Five consecutive configurations are shown for a low-helicity case ($X_0 = 2$). The pattern is asymmetric, requiring eight pulses to return to the initial configuration. The large double-sided arrow at the centre of each configuration indicates the regular rotation of PA in the "torus" region (bins #93–#98). The numbers below each panel enumerate the sequence of pulses.

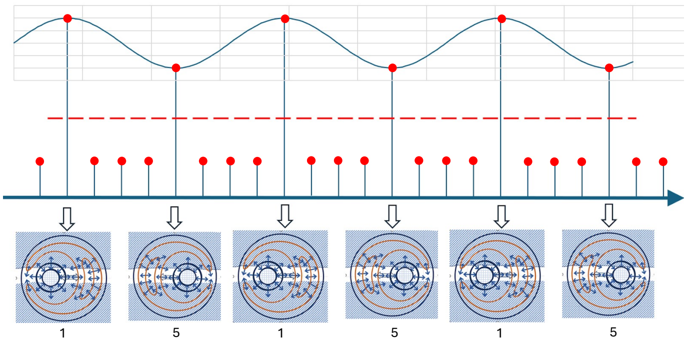

Fig. 14. Model illustrating the behaviour of PLIBs for $P_3 = 4\,P_1$. PLIB pulses exceed the detection threshold and recur with period P_3 (occurrence mode), while their flux is modulated with period $2\,P_3$. The magnetic-flux configurations below each PLIB pulse represent the corresponding emission geometry. The numbers 1 and 5 below each panel correspond to the pulse numbering in Fig. 13. The presented pattern is consistent with a low level of helicity.

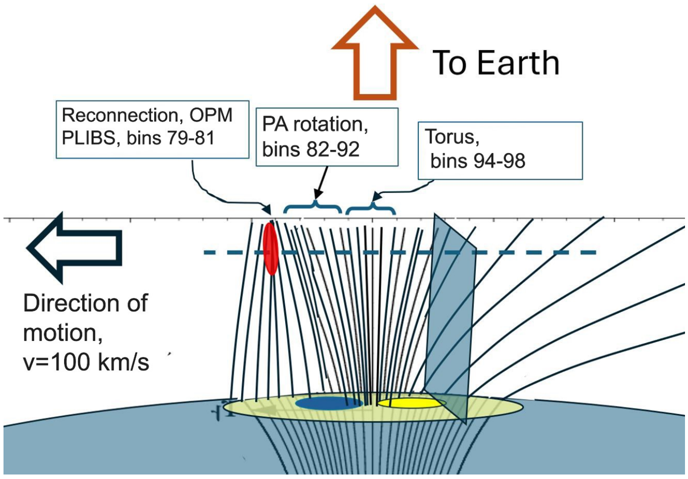

Fig. 15. Schematic illustration of how resistance from the surrounding medium can affect the magnetic-field configuration for a rapidly moving magnetic pole. The magnetic field lines are compressed ahead of the motion and stretched behind it. The blue plane on the right represents an idealised boundary beyond which radiation no longer reaches Earth, due to drag-induced distortion of the magnetic field lines. This magnetic-field configuration leads to the sequential appearance of the observed pulse-phase bins (indicated) within the visibility window. The double-helix structure rotates; in this schematic its orientation is aligned with the velocity vector, corresponding to conditions under which PLIBs and OPM transitions are most likely to occur. This illustration is purely qualitative, not to scale, and the described effects are strongly exaggerated.

caused by the $\mathbf{E} \times \mathbf{B}$ drift of plasma in the polar cap region of a pulsar. The phenomenon of drifting subpulses is explained as a result of spark discharges circulating around the magnetic pole of the neutron star. In contrast, the rotating helix is a direct solution of fundamental equations that describe magnetostatic balance, and bright pulses are a consequence of magnetic reconnection events.

5. Discussion

Phase-locked intermittent brightenings represent a previously unreported form of short-duration emission variability in single-pulse observations of PSR B1919+21. Their defining characteristic is the appearance of transient brightenings confined to a narrow range of pulse longitudes and a limited window of drift cycle phase. Understanding the physical origin of such events requires consideration of both their temporal behaviour and their polarisation properties.

In our analysis we distinguish between two characteristic timescales associated with PLIBs:

1. a long timescale, corresponding to the lifetime of the brightening – the interval during which the bright spot exists within the pulsar emission region – and
2. a short timescale, corresponding to the visibility window – the much shorter interval during which the brightening becomes observable as the pulsar rotation carries it through the line of sight.

The long timescale may be of order P_1 (~1 s or longer), whereas the visibility window within a single rotation lasts only a few milliseconds.

In Sect. 3.1 we showed that PLIB emission is characterised by exceptionally high unpolarised flux. At the same pulse longitude and drift phase, the emission also exhibits unusual polarisation behaviour, including OPM transitions. Such a combination of enhanced unpolarised emission and complex polarisation structure is suggestive of a flare-like release of energy in a turbulent plasma environment.

In this context, the low observed polarisation fraction does not imply intrinsically unpolarised emission, consistent with the expectation that pulsar radiation is generated in polarised modes. Instead, it indicates enhanced depolarisation. In contrast to scenarios invoking large Faraday rotation, such as those observed in some fast radio bursts (FRBs), the effect here is more naturally explained by the superposition of multiple emission components with differing polarisation states.

The polarisation behaviour of PSR B1919+21 itself supports this interpretation. Although the fractional linear polarisation is low on average, the emission exhibits pronounced OPM transitions and rapid variations in both linear and circular polarisation (Olszanski et al. 2022). This combination indicates that the radiation remains intrinsically polarised but is composed of multiple, rapidly varying components whose vector sum reduces the net polarisation.

Within the proposed PLIB framework, magnetic reconnection provides a natural mechanism for producing such conditions. Reconnection is expected to generate a spatially fragmented and dynamically evolving emission region with a broad distribution of magnetic field orientations and plasma properties. Emission from these regions, each polarised but with differing position angles and circular handedness, is superposed, leading to vector averaging of the Stokes parameters and thus to enhanced depolarisation during PLIBs. Finite time resolution can further contribute to this effect, as rapid switching between OPMs leads to additional averaging within a single time bin (Gangadhara et al. 1999), reinforcing the observed reduction in net polarisation.

Sudden changes in pulsar radio emission, including mode switching and nulling, are widely interpreted as manifestations of changes in the global magnetospheric state (Rankin 1986; Lyne et al. 2010). The millisecond-scale brightenings reported here may represent a localised and short-lived manifestation of similar magnetospheric variability occurring on smaller spatial and temporal scales.

The observed association between the appearance of PLIBs and the orientation of the PA of the 'torus' bins (#94–98) also provides insight into the emission geometry. However, caution is required when considering questions of causal ordering. Although we observe an apparent temporal sequence – for example, bin #80 appearing before bin #96 – in the rotating-beam model adopted here the entire emission structure is already present within the pulsar beam; the pulsar rotation simply causes different parts of this structure to be sampled sequentially by the observer. Consequently, the apparent ordering of intensity or polarisation features across pulse longitude does not necessarily imply a causal relationship between them. Within this picture, the brightening, the OPM transition, and the torus-related polarisation features represent coexisting elements of the same emission beam that becomes visible at different rotational phases.

Finally, we note that the reduction of the magnetohydrodynamic equations to a Schrödinger-like eigenvalue problem (Osherovich 1975) suggests that the magnetospheric plasma may admit a discrete spectrum of global eigenmodes. While in this work PLIBs are interpreted within a rotating $m = 1$ configuration, it is conceivable that additional large-scale modes exist and that the magnetosphere may occasionally undergo transitions between such metastable states. A reconfiguration of the global current topology would naturally alter the emission geometry and plasma distribution, potentially manifesting observationally as abrupt profile changes, classical mode switching, or nulling episodes (Rankin 1986; Lyne et al. 2010). Time-dependent simulations further suggest that pulsar magnetospheres can occupy different quasi-stable configurations depending on plasma supply and current closure conditions (Timokhin 2010; Arzamasskiy et al. 2015). In this picture, PLIBs may represent dynamical processes operating within a given eigenmode configuration, while more dramatic phenomena such as nulling or abrupt profile changes could correspond to transitions between different large-scale magnetospheric states.

6. Conclusion

In this study, we identified and characterised a distinct phase-locked emission phenomenon in PSR B1919+21, which we term PLIBs. These events manifest as transient flux enhancements at fixed pulse longitude and drift phase that are consistently accompanied by distinctive polarisation behaviour.

By analysing the distributions of total flux (Stokes I), polarised flux (P), and unpolarised flux ($I_{\rm un}$) over 1,624 pulses, we showed that $I_{\rm un}$ is the most selective and reliable indicator of PLIBs. A threshold at the top 6% of the $I_{\rm un}$ distribution isolates these pulses effectively, whereas thresholds based on total or polarised flux alone fail to do so consistently.

We find that PLIBs are accompanied by a distinctive combination of polarisation phenomena. These include a sharp flare in $I_{\rm un}$ in bin #80 ($l \approx -5°$), an OPM transition between bins #79–80 and #81–82 (corresponding to a 180° rotation in the Q–U plane, or 90° in PA), and a simultaneous reversal in the handedness of circular polarisation, represented by Stokes V.

Folding the PA and $I_{\rm un}$ with a period of $4\,P_3$ confirms that these features recur at a fixed phase within the subpulse drift cycle and are absent elsewhere, demonstrating that PLIBs are not simply brighter instances of ordinary subpulses. Rather, their consistent association with orthogonal-mode switching points to a distinct emission state within the modulation cycle.

Following the occurrence of PLIBs near $l = -5°$, a complete rotation of the PA is observed, corresponding to a 360° rotation of the polarisation vector in the Q–U plane. This full rotation terminates at $l = 0°$ (bin #96), where we previously identified the 'torus' region. This longitude therefore appears to be phase-linked to the bin-80 region and consistently exhibits the same PA as that observed after the OPM transition associated with the PLIBs.

To account for these observational properties, we proposed in Sect. 4 a phenomenological model that builds on the established carousel framework and incorporates double-helix magnetic flux-rope structures (Krat & Osherovich 1978; Osherovich et al. 2013), rotating with the subpulse drift period P_3 or $2\,P_3$. Within this phenomenological picture, the observed millisecond-scale variations in the polarisation pattern do not reflect intrinsically rapid physical changes in the emission region. Rather, they are interpreted as a geometric effect arising from the sequential illumination of the Earth by a narrow radiation beam originating at a fixed altitude in the neutron-star magnetosphere. As different parts of this beam sweep across the line of sight, a quasi-static spatial structure is sampled sequentially in pulse phase, producing the appearance of rapid evolution. In this interpretation, the apparent rapidity is observational rather than physical and is set by the beam sweep rate rather than by the intrinsic timescale of polarisation evolution.

In this framework, spiral distortion of magnetic field lines (analogous to a Parker spiral) and intermittent magnetic reconnection events (Lyutikov 2003; Philippov et al. 2020) provide a plausible qualitative explanation for the key properties associated with PLIBs. These properties include bright unpolarised flares and OPM transitions.

The observed occurrence and modulation patterns further suggest that the underlying double-helix structure is characterised by relatively low magnetic helicity, a condition that may facilitate frequent reconnection events and rapid mode switching. Taken together, these elements form a coherent phenomenological picture linking the polarised and unpolarised emission components and the phase-locked nature of PLIBs within the subpulse drift modulation cycle.

Our results demonstrate that PLIBs – defined observationally as transient, phase-locked brightenings – are not merely enhanced versions of ordinary subpulses but constitute a distinct, phase-coherent emission phenomenon. Their characteristic combination of unpolarised flares, orthogonal-mode transitions, and occurrence within a limited window of drift cycle phase place new observational constraints on models of pulsar magnetospheric structure, mode switching, and plasma dynamics. Future work should aim to test and refine this phenomenological framework through dedicated theoretical and numerical studies, including more realistic plasma physics and self-consistent treatments of electromagnetic fields and particle dynamics.

References

Arzamasskiy, L., Philippov, A., & Tchekhovskoy, A. 2015, MNRAS, 453, 3540
Backer, D. C., & Rankin, J. M. 1980, ApJ, 236, 333
Berger, M. A. 1999, Plasma Phys. Control. Fusion, 41, B167
Bhat, N. D. R., Rao, A. P., & Gupta, Y. 1999, ApJS, 121, 483
Cao, S., Dyks, J., Han, J. L., et al. 2025, ApJ, 983, 43
Castelltort Schnaas, A. 2022, Rangahau Aranga: AUT Graduate Review, 1
Chandrasekhar, S., & Prendergast, K. H. 1956, Proc. Natl. Acad. Sci. USA, 42, 5
Cognard, I., Shrauner, J. A., Taylor, J. H., & Thorsett, S. E. 1996, ApJ, 457, L81
Cordes, J. M. 1986, ApJ, 311, 183
Cordes, J. M., Bhat, N. D. R., Hankins, T. H., McLaughlin, M. A., & Kern, J. 2004, ApJ, 612, 375
Deshpande, A. A., & Rankin, J. M. 1999, ApJ, 524, 1008
Edwards, R. T., & Stappers, B. W. 2003, A&A, 407, 273
Gangadhara, R. T. 1997, A&A, 327, 155
Gangadhara, R. T., Xilouris, K. M., von Hoensbroech, A., & Kramer, M. 1999, A&A, 342, 474
Goldreich, P., & Julian, W. H. 1969, ApJ, 157, 869
Hankins, T. H., & Rankin, J. M. 2010, AJ, 139, 168
Hankins, T. H., Kern, J. S., Weatherall, J. C., & Eilek, J. A. 2003, Nature, 422, 141
Hobbs, G., Lyne, A. G., & Kramer, M. 2004, MNRAS, 353, 1311
Johnson, J., Oberman, C., Kulsrud, R., & Frieman, E. 1958, in Proceedings of the International Conference on the Peaceful Uses of Atomic Energy, Geneva, Switzerland, 1875
Johnston, S., van Straten, W., Kramer, M., & Bailes, M. 2001, ApJ, 549, L101
Johnston, S., Mitra, D., Keith, M. J., Oswald, L. S., & Karastergiou, A. 2024, MNRAS, 530, 4839
Karastergiou, A., von Hoensbroech, A., Kramer, M., et al. 2002, A&A, 391, 247
Krat, V. A., & Osherovich, V. A. 1978, Solar Phys., 59, 43
Li, J., Spitkovsky, A., & Tchekhovskoy, A. 2012, ApJ, 746, 60
Lyne, A. G., & Manchester, R. N. 1988, MNRAS, 234, 477
Lyne, A., Hobbs, G., Kramer, M., Stairs, I., & Stappers, B. 2010, Science, 329, 408
Lyutikov, M. 2003, MNRAS, 339, 623
Lyutikov, M. 2007, MNRAS, 381, 1190
McKinnon, M. M. 2004, ApJ, 606, 1154
McKinnon, M. M., & Stinebring, D. R. 1998, ApJ, 502, 883
Melrose, D. B. 1978, ApJ, 225, 557
Melrose, D. B., & Gedalin, M. 1999, ApJ, 521, 351
Melrose, D. B., & Yuen, R. 2016, J. Plasma Phys., 82, 635820202
Mitra, D., & Rankin, J. M. 2008, MNRAS, 385, 606
Morello, V., Keane, E. F., Enoto, T., et al. 2020, MNRAS, 493, 1165
Navarro, J., Manchester, R. N., Sandhu, J. S., Kulkarni, S. R., & Bailes, M. 1997, ApJ, 486, 1019
Olszanski, T., Rankin, J., Venkataraman, A., & Wahl, H. 2022, MNRAS, 517, 1189
Osherovich, V. A. 1975, Soln. Dann., 5, 70
Osherovich, V. A., Fainberg, J., & Webb, A. 2013, Solar Phys., 284, 261
Oswald, L. S., Karastergiou, A., & Johnston, S. 2023, MNRAS, 525, 840
Pétri, J. 2020, MNRAS, 491, 80
Pétri, J. 2021, MNRAS, 503, 5455
Pétri, J. 2022, MNRAS, 511, 5020
Parfrey, K., Beloborodov, A. M., & Hui, L. 2013, ApJ, 774, 92
Parker, E. N. 1958, ApJ, 128, 664
Philippov, A. A., Timokhin, A. N., & Spitkovsky, A. 2020, Phys. Rev. Lett., 124, 245101
Primak, N., Tiburzi, C., van Straten, W., Dyks, J., & Gulyaev, S. 2022, A&A, 663, A29
Radhakrishnan, V., & Cooke, D. J. 1969, Astrophys. Lett., 3, 225
Rankin, J. M. 1983, ApJ, 274, 333
Rankin, J. M. 1986, ApJ, 301, 901
Romani, R. W., & Johnston, S. 2001, ApJ, 557, L93
Ruderman, M. A., & Sutherland, P. G. 1975, ApJ, 196, 51
Spitkovsky, A. 2006, ApJ, 648, L51
Staelin, D. H., & Reifenstein, E. C. 1968, Science, 162, 1481
Timokhin, A. N. 2010, MNRAS, 408, L41
Uzdensky, D. A., & Spitkovsky, A. 2014, ApJ, 780, 3
van Straten, W., & Tiburzi, C. 2017, ApJ, 835, 293
Wolszczan, A., Cordes, J. M., & Stinebring, D. R. 1984, ApJ, 293, L35
Woolley, M. L. 1975, J. Plasma Phys., 14, 305
Xilouris, K. M., Kramer, M., Jessner, A., et al. 1998, ApJ, 501, 286